Capillary Puddle Vibrations Linked to Casting-Defect Formation in Planar-Flow Melt Spinning

CORMAC J. BYRNE, ERIC A. THEISEN, BARRY L. REED, and PAUL H. STEEN

Planar-flow melt spinning (PFMS) is a single-stage rapid manufacturing/solidification technique for producing thin metal sheets or ribbons. Molten metal is forced through a nozzle onto the substrate where it freezes and is spun as ribbon product. A puddle of molten metal held by surface tension (capillarity) forms between the nozzle and substrate. An important measure of product quality is the uniformity of thickness along and across the ribbon. At small length scales, local thickness changes or surface defects are present that are undesirable. This work examines the cross wave, a well-defined periodic surface defect, seen when casting aluminum-silicon alloys. The presence of the defect is related to processing conditions and puddle dynamics. Motions of the puddle menisci are captured using high-speed video and analyzed for frequency content. A high frequency vibration of both menisci corresponds to the observed frequency of the surface defect. A scaling analysis reveals these motions to be capillary in nature and comparisons are made with two model problems of vibrating capillary liquids.

I. INTRODUCTION

PLANAR-FLOW melt spinning (PFMS, also known as planar-flow or single-roll spin casting) is a continuous casting technique for rapidly solidifying thin metal sheets or ribbons. The technique has been of interest (1) because of the economic and environmental advantages of casting a final product directly from the melt and (2) because of the special properties arising from the unusual microstructure of rapidly frozen alloys. For ribbons cast thinner than 1 mm, present bench-scale machines, including ours, make product at economically attractive rates but of insufficient quality. Our goal is to develop a scientific understanding of various undesirable features appearing in the product so that these may be eliminated or, at least, manipulated, and the quality thereby enhanced.

We cast aluminum (and Al alloys) into ribbon of 50-mm width (not limiting) and 0.1-mm thickness, typically. The distinction between surface and bulk features blurs at this thinness. A charge of 1 kg yields a ribbon of nearly 75-m long at these dimensions. A typical casting speed is 10 ms^{-1}. Note that our casting speed is an order of magnitude faster and our thickness an order of magnitude thinner than the state-of-the-art for commercial casting.[1]

The focus of this article is an imperfection that crosses the ribbon product spanwise with a regular streamwise spacing. The marks are easily observable on both top and bottom surfaces with the naked eye. The ''cross-stream wave,'' as it is sometimes referred to, arises over a broad range of conditions and has been reported in other studies.[2,3] It is observed by laboratories casting a variety of alloys. The thrust of this article is that this wave defect ultimately arises from the oscillation of the molten metal puddle at a natural frequency determined by the balance between liquid inertia and surface tension. Such a mechanism is consistent with the prevalence of the defect. Previous work has speculated about the role of the free-surface meniscus in the formation of such features.[4,5] The present work establishes the link with a particular puddle vibration.

The PFMS has been studied extensively over the two decades following 1975, driven mainly by an interest in the enhanced magnetic and mechanical properties that rapidly quenched materials can have due to their microcrystalline or amorphous microstructures. Early reviews dealt with the material properties of the melt-spun product with some focus on processing issues.[6,7] The fluid flow came into focus later.[8] A review of the process fluid mechanics is available.[9] More recently, combinations of numerical and experimental studies have appeared.[10,11] Other work has focused on correlating processing parameters with ribbon quality and dimensions.[3,4,12,13] Many authors have reported surface features including herringbone patterns, dimples, striations in the cast direction, and cross-stream waves, but mechanisms of formation have not been identified.[2,3,13]

Thickness variations in the product cast in our laboratory are seen at various length scales. The cross-stream wave corresponds to typical thickness variations of about 30 pct of the mean (for ~150-μm-thick ribbons). This type of feature is persistent in our cast ribbons (aluminum alloy) and is detrimental to the integrity of the product. With a nominal Al-7 pct Si alloy, the presence of the cross-stream wave reduces the ultimate tensile strength by 20 to 30 pct on average, for example.

The cross-stream wave is shown in Figure 1. The feature is apparent as a wavy line running across the width of the ribbon in these photographs. The wave has a well-defined wavelength λ, on the order of 1 cm, in the cast direction. A composite image of both the substrate and free side of a sample of ribbon, made using a MicroXam Interferometric Profilometer (ADE Phase Shift, Tuscon, AZ), is shown in Figure 2. Two waves appear in this sample of ribbon. The average thickness of the sample is approximately 180 μm.

CORMAC J. BYRNE and ERIC A. THEISEN, Graduate Students, and PAUL H. STEEN, Professor, Center for Applied Mathematics, are with the School of Chemical and Biomolecular Engineering, Cornell University, Ithaca, NY 14853. Contact e-mail: phs7@cornell.edu BARRY L. REED, Scientist, is with the Center for Naval Analyses, CNA Corporation, Alexandria, VA 22311.

Manuscript submitted July 7, 2005.

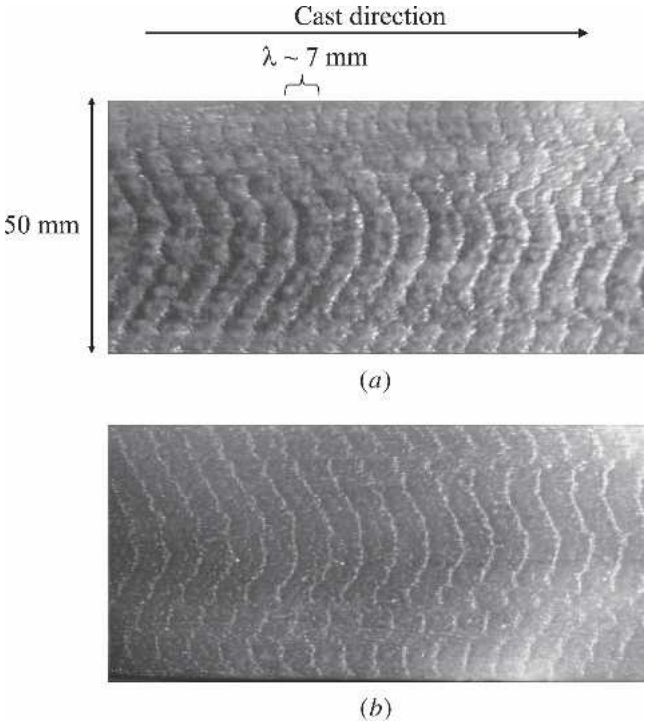

Fig. 1—Photograph of the cross-stream wave as seen on (*a*) the free side and (*b*) the substrate side of the ribbon product. The wavelength $\lambda \approx 7$ mm is seen on a ribbon section, 50 × 130 mm. The cast direction is left to right.

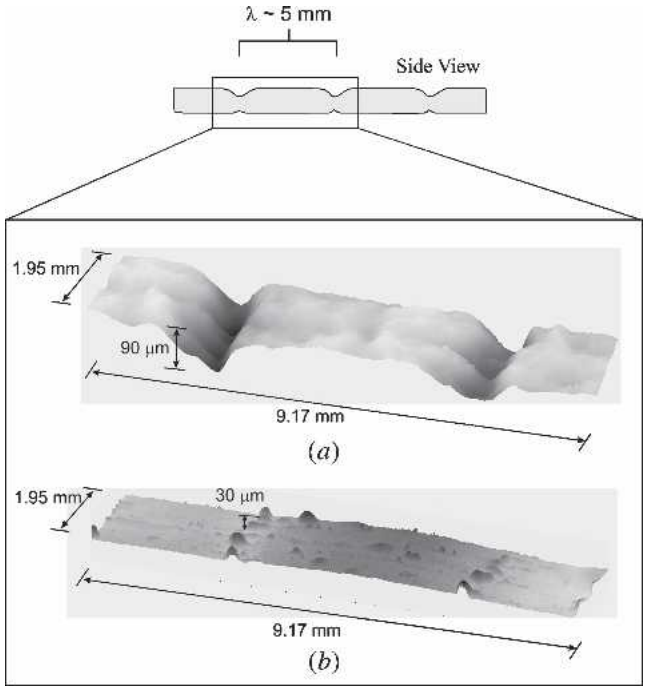

Fig. 2—Profile of ribbon surfaces. (*a*) Scan of the free side showing two cross waves. (*b*) Scan of substrate side. Schematic on top shows the location of the scans on the ribbon. The craters and trenches extend into the solid product. Notice that the vertical lengths have been expanded for clarity.

On the free side (Figure 2(a)), the thickness reduction resembles a continuous trench. The surface between the wave crests is relatively uniform when compared to the depth of the trench. On the substrate side (Figure 2(b)), what appears as a valley in Figure 1(b) is actually a concentration of craters. The crater depth can be as great as 30 μm for this sample. A small number of randomly distributed craters of lesser depth may also be present between waves on the substrate side. However the surface between defects is relatively flat. The defect is in registry between the substrate and free side. That is, there is no measurable horizontal displacement of the trench on the top with respect to the row of craters on the bottom.

A variety of similar surface features have been reported in other continuous casting processes. The origin of short wavelength thickness variations in melt overflow casting of aluminum has been discussed.[14] These variations have been interpreted as being a result of repeated meniscus pinning/depinning. Also, the presence of substrate velocity-dependent cross-stream defects in melt drag twin roll casting has been attributed to the bouncing of the meniscus at the nozzle tip.[15] The appearance of so-called ''oscillation marks'' on continuously cast steel slabs is well documented. The frequency at which these oscillation marks appears is directly related to the mold oscillation frequency. It has been suggested that several mechanisms may act together to form the oscillation marks, including meniscus freezing and overflow as well as thermal stresses in the solidifying material.[16,17] In most instances, the marks are removed by shaving the finished product.

Periodic cross-stream waves are also seen in many liquid film coating processes. Among these processes, slot coating stands out as having a geometry and operating configuration similar to PFMS. The key differences with PFMS are (1) that solidification occurs downstream of the puddle in typical coating flows and (2) that viscosity plays a dominant role in many coating operations, whereas, in PFMS, the high speed of material deposition makes the flow largely inviscid. Nevertheless, it is well recognized that meniscus and wetting-line stability influence the surface of the coating products.[18] Cross-stream periodic bands are observed for a variety of coating processes. These bands are often attributed to the movement of the wetting line.[19] Even though it is not known to what extent puddle oscillations are related to any observed coating flow instabilities, it is instructive to use coating flows for contrast.

In Section II, we distinguish two formation mechanisms for periodic features frozen into the cast product. Section III describes the process and parameters in detail. In Section IV, we provide the experimental evidence that the cross wave correlates to motions of the menisci. A correlation between the menisci motions and the main processing parameters is given in Section V. A competition between capillary and inertia effects sets the time scale for the motions. In Section VI, we briefly discuss parameter regimes where the cross wave is not observed. Finally, Section VII compares related observations from the literature to the oscillation of an inviscid sphere and a meniscus moving in a channel between parallel plates. Additionally, we propose that heat-transfer interruptions are a likely mechanism by which puddle vibrations turn into thickness variations in the product.

II. TEMPLATE VS PULSE TRANSFER

For any feature with a characteristic streamwise wavelength on a continuous cast product, one can distinguish two fundamentally different mechanisms of formation. In the first, a pattern on the substrate is transferred directly onto the solidified product, much like what occurs in contact printing where inked type is pressed against a paper substrate to produce a printed page. In this case, the spacing of the template (substrate) is transferred directly to the product. Double the speed of the substrate and the spacing of the lines on the printed page remain unchanged. For a substrate moving at speed U, the wavelength λ does not depend on U. We shall call this *template-transfer* formation. In the second mechanism, the wavelength is created by a constant-frequency oscillation in the lab frame, much like what would occur by inkjet droplets impinging on a moving substrate from a source of fixed frequency. Doubling the substrate speed will double the wavelength of the feature since the substrate moves twice as far between impingement events. In other words, λ is linear in U ($\lambda \sim U/f$). We shall refer to this as *pulse-transfer* formation. The dependence or not of λ on wheel speed will be key to identifying the physics of cross-wave formation.

A distinct issue is how to report the measured λ of periodic features. It can be reported directly as λ or as an inferred frequency:

$$f_\lambda \equiv U/\lambda \qquad [1]$$

These are entirely equivalent measures, of course. However, it should be kept in mind that for different measures the dependence on wheel speed is different for the same formation mechanism. For example, for template transfer, f_λ is linear in U while λ is independent of U, and, for pulse transfer, the opposite is true. We shall mostly report data in terms of f_λ, except for the final correlation over a large range of cast ribbons in which case we shall use λ.

III. APPARATUS AND EXPERIMENTAL METHODS

Figure 3(a) shows a schematic of the casting apparatus, which comprises a crucible for housing the molten metal, a nozzle through which the metal can flow, and a metallic substrate (or chill wheel). An inert gas pressurizes the crucible in a way that compensates for the decreasing metallostatic head as the metal flows out. Our experimental caster operates using a 1-m-diameter Cu-Be substrate. A blowup of the region between the nozzle and substrate, or contact zone, is shown in Figure 3(b) (horizontal lengths are compressed for clarity). The process feeds molten metal from the crucible (due to a combination of head and applied gas pressure) through the nozzle of breadth, B, into the thin gap region between the nozzle and substrate. The pressure at the nozzle entry to the puddle ΔP is held constant during a cast by the pressure compensator mentioned previously. Because of the small gap G, the nozzle interferes with the flow and a puddle, held by surface tension, is formed. The contact between the substrate and molten puddle is such that enough heat is removed from the melt for solidification to occur. Material solidifies along a front at an average velocity V. The substrate (moving with linear velocity U) continually removes the solidified product from the melt puddle. The final ribbon thickness T depends mainly on the five parameters B, G, ΔP, V, and U. Mass, momentum, and energy balances with appropriate boundary conditions have been written down and put in nondimensional form elsewhere,[20] accounting for the effects of the parameters listed in Table I. It is learned that, for operating parameters typical of our experiments, the momentum transfer problem depends on the heat-transfer problem but not *vice versa* (one-way coupling). The thermal control parameters for the experiments reported in this article are fixed; only the mechanical control parameters are varied and the influence on the mechanical problem is parametric through V and indirectly through G (it changes with time due to wheel heatup). The experimental casting apparatus in our laboratory is described in detail elsewhere.[13,21,22]

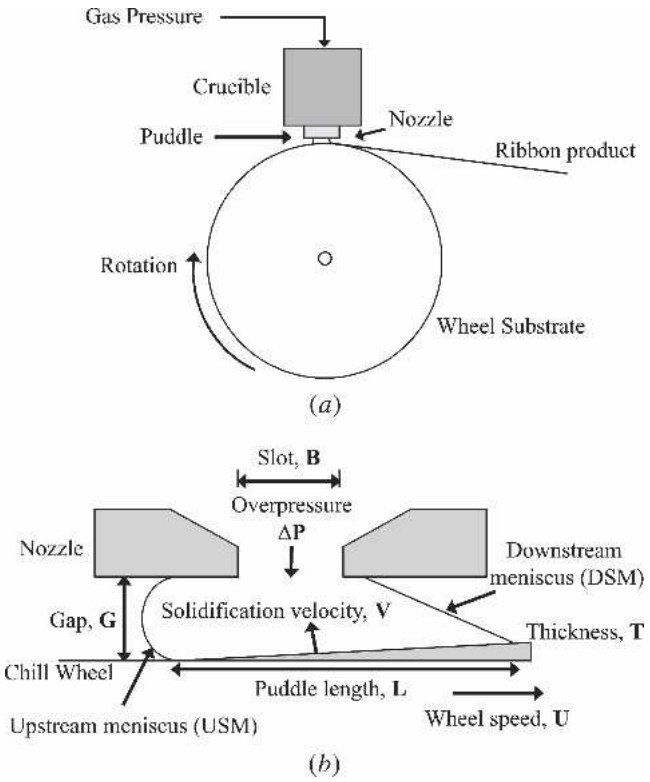

Fig. 3—(*a*) Schematic of the PFMS apparatus. Metal is poured from the crucible through a nozzle onto the spinning substrate or chill wheel, where it forms a puddle. Solidification occurs and a ribbon of thickness T is pulled from the puddle and thrown from the substrate. (*b*) Blowup of the contact zone or puddle region. The horizontal length scale has been compressed.

The range of typical values for processing parameters and variables are given in Table I. Successful casting occurs only for certain "stability windows" within parameter space. Although steady behavior does not depend on surface tension σ, the limits of steady behavior (stability window) do. All data reported subsequently came from experiments carried out in these ranges. Puddle length L and solidification rate V are included as process variables, but they are not actually set by the operator. Specific cast data can be found in the Appendix.

Figure 4 shows the ribbon thickness T, wavelength of the cross-wave λ, and gap spacing G, as they vary throughout

Table I. Process and Material Parameters with Typical Values

	Nozzle Geometry	
G	0.5 to 1.3 mm	range of nozzle/wheel gaps
B	1.6 to 3 mm	nozzle slot breadth
W	25 to 50 mm	nozzle slot width
	Process Variables	
T	0.08 to 0.35 mm	range of ribbon thickness
L	4 to 20 mm	typical range of puddle length
U	5 to 15 m s^{-1}	wheel speed (linear)
ΔP	4×10^3 N m^{-2}	overpressure
V	0.05 to 0.1 m s^{-1}	solidification rate
T_h	1033 K	superheat temperature
T_c	298 K	quench temperature
	Material Properties (Aluminum Unless Otherwise Noted)	
ρ_s, ρ_l	2.7×10^3, 2.3×10^3 kg m^{-3}	solid, liquid density
k_s, k_l	229, 103 J m^{-1} s^{-1} K^{-1}	solid, liquid thermal conductivity
η	10^{-3} kg m^{-1} s^{-1}	viscosity (1033 K)
σ	0.86 N m^{-1}	surface tension (1033 K)
T_m	933 K	melting temperature

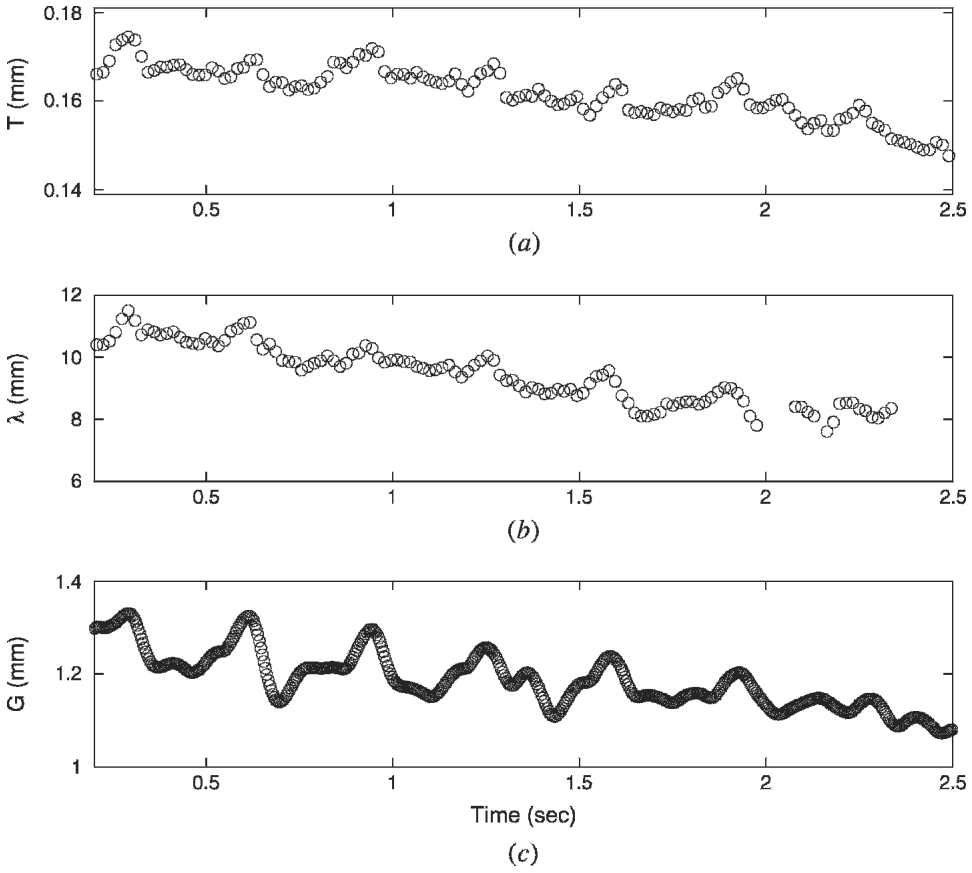

Fig. 4—The evolution of (*a*) ribbon thickness, (*b*) defect wavelength, and (*c*) gap spacing through a cast with ΔP held constant. Note the gradual decrease in these values due to thermal expansion of the substrate. The periodic behavior is due to the out of roundness of the substrate. A five-piece moving average has been applied to the data for clarity.

the duration of a cast. This particular cast is some 20-m long. Each thickness and wavelength data point represents a value found from averaging over a 0.15-m length, obtained as follows. The ribbon is cut into a number of 0.15-m-long pieces. For each piece, the thickness is measured from the mass and area (reported in Figure 4(a)) and the average wavelength by dividing the 0.15-m length by the number of waves present (reported in Figure 4(b)).

Figures 4(a) and (b) indicate variations in thickness and wavelength that occur on two length scales larger than the piece size. First, over the total length of the cast (the largest scale), there is a gradual downward trend. Second, there is a periodic variation on the lengthscale of the wheel's circumference (about 3 m). The gradual decrease in thickness has been shown to be the result of wheel heatup. The wheel average heatup has been measured at about 50 °C to 80 °C for typical 5-s casts.[23] Wheel expansion decreases the gap G, increasing the hydrodynamic resistance to flow, and hence decreases the flow rate, in view of the constant applied pressure drop ΔP.[21] The shorter-scale variation shown in Figures 4(a) and (b) is directly related to the out of roundness of the substrate, which changes G periodically. Indeed, the period of the oscillation matches the time required for one revolution of the wheel.

The sources of both these long lengthscale variations are mechanical and due to time-dependent forcing of the gap. That is, a $G(t)$ is imposed; template transfer occurs. The before-cast hot gap $G(0)$ is known to within ± 5 pct of the desired G. The change in G throughout a cast is measured by using a run-out meter placed on the substrate. This allows for $G(t)$ to be measured to within ± 5 pct. One such $G(t)$ is shown in Figure 4(c). Both a gradual decrease and periodic variation on this trend are evident in these data. Note that values presented in Figure 4 represent a moving average over ~0.07 seconds (five ribbon pieces), done to smooth very local variations.

We will report both gap G and wavelength λ values in this study. A series of instantaneous values taken at subsequent instants throughout the cast will be referred to as *pointwise* data, while averages of such a series over the entire cast will be called *cast-averaged* values. Values of G reported below are ''cast averaged'' unless noted as pointwise. An example of pointwise values is given by the data points in Figures 4(b) and (c). It is impractical to measure $G(t)$ directly for every cast so a means was developed to infer the shrinkage over the duration of a cast, as described in the Appendix. This allows us to apply an average decrease to subsequent experiments carried out under similar conditions. The error introduced by this approximation is ± 10 pct.

IV. PUDDLE OSCILLATIONS

Video imaging of the puddle indicates that the upstream meniscus (USM) and downstream meniscus (DSM) are moving throughout the entire cast. Motions are captured by a Kodak (Rochester, NY) EktaPro high-speed video system. A high-intensity fiber optic light is used to locally backilluminate the desired meniscus. The high-speed video system, capable of recording at up to 6000 frames per second, is focused on the profile of the meniscus region. Focusing on the menisci rather than the entire puddle region has allowed much smaller motions of the menisci to be observed than previously reported.[4,22,24] Several regimes of motion of the menisci are identified from these images. These are shown schematically in Figure 5, along with still images of the USM and DSM taken from video. The motions are distinguished as follows.

(A_1) A large scale left-right mean motion of the USM. That is, the mean position of the meniscus moves. This mode is the slowest of those observed. (A_2) For any mean position of the USM, there are time-dependent bulk deformations superposed on the mean. These are also left-right in nature, but faster than A_1. (B) Traveling waves on the DSM, similar to those reported previously.[4]

In Figure 5, only a portion of the DSM is shown. These traveling waves originate at the nozzle-liquid-air contact line (top) and travel toward the liquid-solid-air trijunction (below). In all observed cases, their amplitude decreases as they travel downward. This is consistent with solidification being completed within the puddle region by the time the last molten metal reaches the liquid-solid-air trijunction.

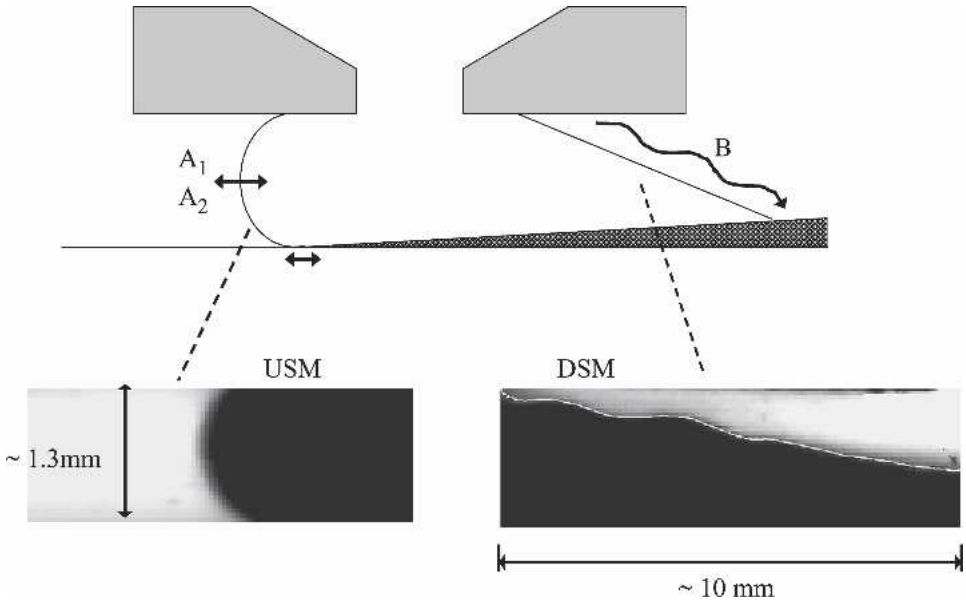

Fig. 5—Types of puddle motions. A_1 is a large-scale left-right motion of the USM, while A_2 is a smaller scale left-right vibration of the USM. The term B represents waves on the DSM. A white line is fitted to the edge of the DSM for clarity. Notice the different length scales associated with the photographs.

As seen in Figure 6, the USM is asymmetrical about the midplane, being dragged under by the moving substrate. Visualization of the motion of the lower dynamic contact line has had limited success due to the difficulty in illuminating the inner contact region. Figure 6 shows images of the USM over one period of the oscillation illustrating motions of the type A_2. Notice how the shape of the USM deforms or ''wobbles'' as the liquid-substrate contact line pulls to the right (in the direction the substrate is moving).

To quantify these motions, a time series of the displacements of the puddle menisci are extracted from the high-speed video (a threshold technique with linear interpolation yields subpixel resolution[25]) and analyzed for frequency content by fast Fourier transform. For brevity, we only present data here that relate to motions of type A in Figure 5. Frequencies for motions B are similar to those for motions A.

A typical time series of the motions A, for $G = 1.3$ mm, is shown in Figure 7(a). This plot is of the motion of the left-most point on the USM relative to the right edge of the image, which is fixed in space. Motions of different amplitudes are seen. The longest periodic motion shows approximately nine large peaks over a 1-s period (motion A_1). Superimposed on this is a smaller amplitude and higher frequency motion, which is enlarged in Figure 7(b) (motion A_2). On the vertical axis, one arbitrary unit corresponds to approximately 30 μm of motion of the puddle interface. Note that Figure 7(a) shows nine peaks during 1 second while Figure 4 shows only three peaks. The data come from casts at essentially the same wheel speed. The difference is the moving average applied to the data in Figure 4; it is done over five pieces (0.75 m) or about one-quarter of the wheel circumference. Thus, since every hill has an adjacent valley and the averaging window always includes a hill/valley pair, the smaller two of the three hills on the wheel get averaged out in Figure 4.

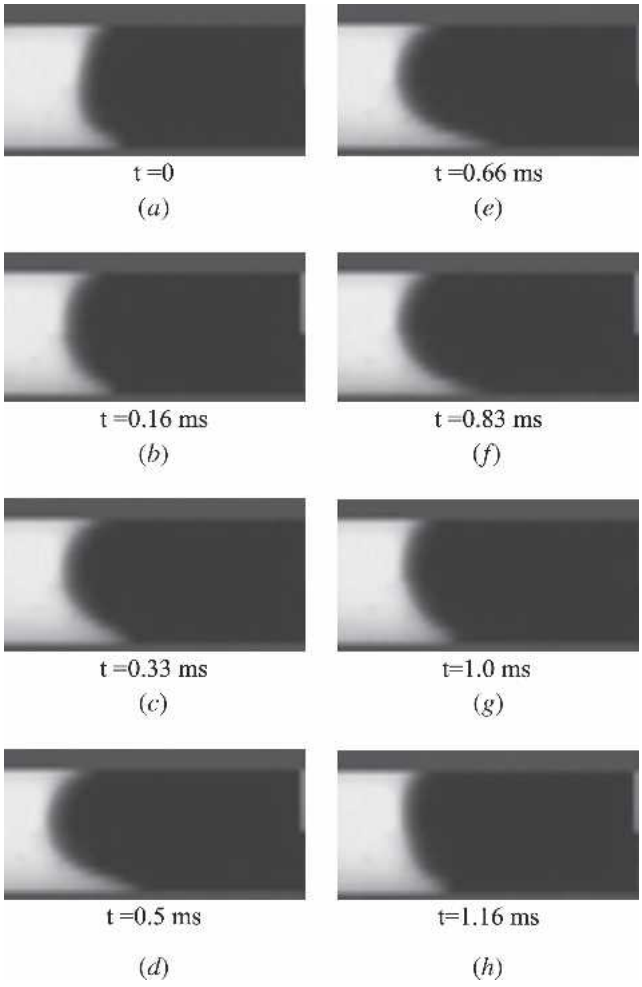

Fig. 6—Images of the USM motion over one period of oscillation. The meniscus is initially seen to be flat ($t = 0$ ms) and then deforms as the contact line moves in the direction of the translating substrate. Eventually, the contact line moves back to approximately its original position ($t = 1.16$ ms). The gap spacing is approximately 1.3 mm.

The power spectrum of the data in Figure 7(a) is shown in Figure 7(c). The data were taken to capture the higher-frequency oscillation f_2 at about 800 Hz. The lower frequency f_1 just shows up, nevertheless, at about 9 Hz. It has an amplitude several orders of magnitude greater than f_2. This is in agreement with observations from the raw time series. A slight anomaly is just visible around 1600 Hz. This is the second harmonic of f_2. The power spectra for motion B show identical peaks at f_1 and f_2.

A series of experiments were carried out using different values of G while keeping U fixed (Table II). It is observed that as G is changed the value of f_1 remains constant. In contrast, f_2 varies with G. Also included in the table are corresponding wave frequencies, f_λ, as inferred from the cast-averaged λ measurement. Since the gap varies continuously, the frequency also varies along the length of the ribbon, and this nonstationary behavior gives an error associated with f_λ. The reported f_λ is the average value $\pm$ the standard deviation. The secondary frequency f_2 appears for all gap heights exceeding $G = 0.53$ mm. For $G = 0.53$ mm, no cross-stream waves were present on the ribbon.

It should be noted that the peak centered about f_2 in Figure 7(c) is rather broad. This is the case in all power spectra from which the f_2 values reported in Table II were taken. The out of roundness of the substrate is responsible for the broadening of this peak (this can be confirmed using Eq. [3] in Section V). The salient feature is the maximum value (reported as f_2). The values of f_2 and f_λ are nearly the same and consistent with the common source of broadening and have similar standard deviations.

V. CROSS-WAVE PHYSICS

The lower frequency f_1 relates directly to the out of roundness of the substrate. Based on the characteristic substrate speed of Table II ($\sim$8.8 m/s) and the known topography of the substrate, a periodic gap variation of approximately 9 Hz is expected. Experiments at different wheel speeds are shown in Table III. Note that f_1 increases linearly as the substrate speed is increased. Comparing U and f_1 values indicates that the wavelength of the topographical features on the substrate is approximately 1 m corresponding to three hills per circumference; this has been verified by direct measurement of wheel topography. It is apparent that the puddle is oscillating at this frequency to accommodate the gap variation. Therefore, frequency f_1 reflects a template-formation mechanism.

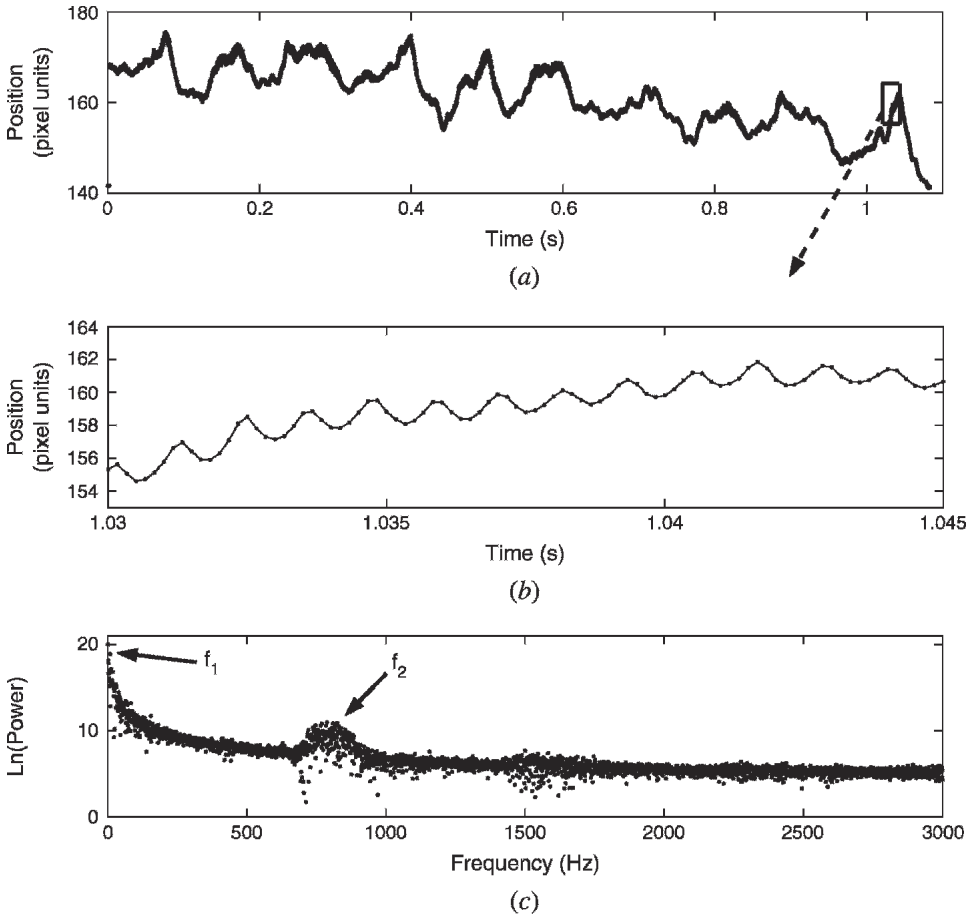

Fig. 7—(*a*) A time series of USM motion (type A) for $G = 1.3$ mm. On the vertical axis, one unit corresponds to approximately 30 μm of motion. (*b*) An expanded view of a smaller portion of data shows the small-scale motions. (*c*) The power spectrum of data (notice the log scale on the *y*-axis).

Table II. Summary of f_1, f_2, and Average Cross Stream Wave Frequency ($f_\lambda \equiv U/\lambda$) for Different Cast-Averaged G Values

G (mm)	f_1 (Hz)	f_2 (Hz)	f_λ (Hz)
0.53	9	—	—
0.78	9	1450 ± 200	1500 ± 185
1.1	9	960 ± 90	950 ± 80
1.3	9	800 ± 60	790 ± 50

We turn to the frequency f_2. As shown in Table II, values for f_2 coincide with the measured cross-stream defect frequency f_λ. That is,

$$f_\lambda = f_2 \qquad [2]$$

This frequency increases with decreasing gap height G. In contrast, Table IV, shows three separate casts with cast-average $G = 1.3$ mm and where U is varied. It is observed that λ varies such that f_λ remains approximately the same (within the experimental error). We conclude that f_λ is independent of U and arises from oscillations in the lab frame of fixed frequency. Hence, λ *and* f_2 result from a pulse-transfer mechanism.

As just described, f_λ varies with G but is independent of U. A log-log plot shows that $f_\lambda \sim G^n$, where $n \sim 1.42$. To avoid casting failure, parameter variation must remain within the stability window.[13] For this reason, less than a decade of G is tested to determine n. Hence, the power-law exponent must be interpreted cautiously. To probe how f_λ changes with other processing conditions, 34 casts are compared. Associated conditions are listed in Table V of the Appendix. Processing conditions vary within the ranges listed in Table I. Cross-wave frequency f_λ is found *not* to correlate with ΔP, B, or W.

Table III. Behavior of Frequency f_1 as the Wheel Speed U is Varied

G (mm)	U (m s^{-1})	f_1 (Hz)
1	14	14
0.8	11.9	12
0.8	8.8	9
0.8	5.7	6

Dimensional reasoning using the observations of the last paragraph suggests that f_λ be scaled with a capillary time scale $\tau \equiv (\rho G^3/\sigma)^{1/2}$, where ρ is the liquid density, σ is the surface tension, and G is chosen as the characteristic length scale. That is, generally, one expects $f_\lambda \tau$ to depend on the dimensionless control parameters, say, $f_\lambda \tau = g[\Delta P/\rho U^2, G/B, G/W]$. However, observations, including those mentioned previously, suggest that the function g is in fact

Table IV. Summary of f_λ as the Wheel Speed U is Varied

G (mm)	U (m s^{-1})	λ (mm)	f_λ (Hz)
1.3	7.1	8.6 ± 0.6	825 ± 54
1.3	8.8	11 ± 0.9	800 ± 60
1.3	11.9	14.5 ± 1.3	821 ± 68

a constant, to the accuracy of our measurements. In other words,

$$f_\lambda = C\left(\frac{\sigma}{\rho G^3}\right)^{1/2} \quad [3]$$

Here, C is a proportionality constant. For a given alloy (fixed σ and ρ), the frequency of capillary oscillations depends only upon G. There are two approaches to extracting C from the experimental data. The first is to use pointwise values of G, λ, and U, while the second is to use cast-averaged values. It will be shown that these two methods yield the same value for C.

Gap G varies throughout the time of the cast and can be measured directly using a run-out meter placed on the substrate, as discussed in Section III. For three different casts, these time-dependent values for λ and G are used to plot f_λ against $(\sigma/\rho G^3)^{1/2}$ (Figure 8). A linear regression is applied to all the data to yield $C \sim 1.9$. In each of the three casts, G decreases by about 30 pct throughout the cast consistent with wheel heatup.

Next, the correlation is tested over a broader range of U and G by cast-averaging ($\approx$4 seconds) a series of casts. Using Eq. [1], Eq. [3] can be rearranged to yield

$$\lambda = \frac{U}{C}\left(\frac{\rho G^3}{\sigma}\right)^{1/2} \quad [4]$$

In Figure 9, 34 separate casts are reported. The value of G is varied between 0.78 and 1.3 mm, U is varied from 5 to 15 ms^{-1}, B is varied from 1.6 to 3.2 mm, and W is varied from 25 to 50 mm. Each data point represents a cast-averaged value. The main advantage here is that of statistics; each data point represents an average of some 200 pointwise wavelengths (one per piece). The solid line gives the prediction of Eq. [4]. In summary, it is observed that $C = 1.9$ correlates the values of λ over a broader range of U and G using cast-averaged values than seen in the pointwise correlation of Figure 8. The combined uncertainty in the G and λ data is about ±10 pct. Most data points fall well within this uncertainty and representative error bars are plotted for two data points.

The surface tension σ is an important factor in the capillary oscillation of the puddle. By varying σ, the scaling predicted by Eq. [4] can be further tested. The surface tension of a liquid metal can be varied in two ways: (1) by changing the temperature of the liquid and (2) by varying the composition of the material.

The surface tension of Al has a weak dependence on temperature and the superheat for our casting procedure is modest (nozzle temperature of ~700 °C and melting temperature above 600 °C). Hence, compositional variation was explored. The surface tension of Al alloyed with Si does not vary significantly.[26] However, by adding small amounts of bismuth (Bi), σ can be reduced by up to 50 pct.[26] An alloy of composition Al-7 wt pct Si-4 wt pct Bi (±0.3 wt pct) was prepared from Al-Bi and Al-Si master alloys. Several published works indicate that the surface tension of this alloy, at a temperature of approximately 700 °C, is 0.48 ± 0.02 Nm^{-1}, reduced from a value of 0.85 ± 0.02 Nm^{-1} for the regular Al-7 wt pct Si alloy.[26,27] This lower surface tension alloy was cast twice at different U and these data fall nicely on the correlation in Figure 9, indicating that the wavelength of the defect adjusts to compensate for the changing surface tension. In summary, the correlation has been tested by varying G, U, and σ, three of the four variables that enter the abscissa of Figure 9 (varying ρ is not feasible). This directly confirms the capillary nature of the vibrations.

VI. THRESHOLDS FOR CROSS-WAVE APPEARANCE

The cross-stream wave, while persistent under most processing conditions, does not appear when (1) casting below certain values of U or G, (2) casting nominally pure Al, or (3) the puddle is overly constrained.

As noted in Section IV, the cross-stream wave is not observed for low gap settings. That is, for a fixed U, reducing the gap setting will eliminate the cross-stream wave. This critical gap was found to be approximately 0.6 mm for $U = 8.8$ ms^{-1}. Similarly, for a fixed G, reducing U will also suppress the wave. For example, with $G = 1.0$ mm, the critical value of U is approximately 5 ms^{-1}.

The cross-stream wave can also be eliminated by casting nominally pure Al. For Al-Si alloys, more than approximately 2 pct Si is needed for the wave to appear. However, for percentages of Si in the melt above 2 pct, the defect wavelength is independent of the alloy composition.[21] That is, λ for Al-3 pct Si is the same as that for Al-9 pct Si. Nominally pure Al casts (<2 pct Si) do not show a cross-stream wave, but rather quite often contain a shorter wavelength ($\approx$1 mm) defect known as the herringbone pattern. This herringbone pattern is a series of fine lines on both sides of the ribbon and has been reported elsewhere.[2,13] The Al-Si casts are mostly 7 pct Si in Al, but the wave is also present in a range of other alloys that we have cast. These include Al-7 pct Si-4 pct Bi, as well as the A356 and B356 alloys.

Geometric differences in the puddle may also result in ribbons that do not show the cross-stream wave. It has been found that the wavelength of the defect has no dependence on the overpressure ΔP when all other parameters are fixed. However, when ΔP is so low that the puddle takes the constrained configuration of Figure 10(a), the defect is not observed. The herringbone pattern is dominant in this product. During casts where the downstream detachment point is pinned at the edge of the nozzle, as shown in Figure 10(b), and the DSM tends to bulge out, the cross-stream wave is also not observed and the herringbone pattern can appear. Nominally pure Al casts almost always take this configuration and Al-Si casts can be forced to do so. Typically, the contact lines in regular Al-Si casts are free to

move and take up positions midway between the slot and the nozzle edge, as illustrated in Figure 5. This additional degree of freedom for motion of the puddle may be significant in terms of the modes at which the puddle can vibrate.

VII. DISCUSSION

In this section, we shall first reaffirm the appropriateness of the scaling found in Section V. We shall then briefly compare our measured frequencies with predictions of two model problems of inviscid capillary vibration: the spherical interface and slot meniscus. Our results will then be contrasted to related observations from the literature. Finally, we offer some remarks on how the puddle oscillation may freeze into the cross wave shown in Figure 2, the question of mechanism.

The molten metal puddle oscillates at two distinct frequencies. The first (≈10 Hz) corresponds to a large motion of the puddle forced by a periodic variation of the gap height, whose source is the topography of the moving substrate. The second is a vibration (≈1000 Hz) that corresponds to the natural frequency of liquid inertia countered by surface tension. The source of this puddle vibration is fixed in the lab frame. Since the cross-stream wave in the cast product correlates with the higher frequency, our focus is there.

The surface tension force σW acting per unit width W of the puddle is σ. To estimate the rate of change of momentum per unit width (mass/length × velocity/time), one needs an estimate of the volume participating in the oscillation (from which the length scale for the velocity follows, or *vice versa*). The volume could be GLW or G^2W depending on the motion. Observation (*e.g.,* Figure 6) suggests that the velocity is G/τ and hence that the appropriate volume is G^2W. This is similar to the slot meniscus model discussed subsequently for which the liquid has volume GLW but a volume within a distance G of the meniscus essentially participates in the vibration (volume G^2W). The appropriate balance between inertia and capillarity is then $\sigma \sim \rho G^3/\tau^2$ from which emerges the capillary time scale $\tau \sim (\rho G^3/\sigma)^{1/2}$. Finally, the fact that the coefficient-of-proportionality C in correlation 3 turns out to be order 1 suggests that the chosen scaling is indeed appropriate.

It is instructive to compare this finding with the classical problem of a liquid sphere of diameter G and density ρ, held by capillarity (tension σ) and surrounded by a passive gas (removed from gravity).[28] If the sphere is slightly deformed and then released, it oscillates with distinct mode shapes at corresponding frequencies. The eigenfrequencies are

$$\nu = C_\nu \left(\frac{\sigma}{\rho G^3} \right)^{1/2} \qquad [5]$$

where the constant C_ν depends on the mode number and $C_\nu \approx 1.27$ for the lowest harmonic. Compare this result to $C_\nu \approx 1.9$, found in correlation [3]. Furthermore, the corresponding modal deformation from oblate to prolate spheroid and back again is shared by the shape change seen in Figure 6.

A meniscus holding an inviscid liquid in between two parallel plates, separated by a distance G and closed on one end, also oscillates with a frequency given by Eq. [5]. This configuration more closely approximates the constrained geometry of the puddle in PFMS. In this case, in addition to the mode number, the constant C_ν depends on the volume of liquid and the angle at which it meets the plates. Myshkis *et al.*[29] has solved this problem for the case of fixed contact-angle boundary conditions (moving contact line). For a contact angle of about 140 deg (estimated from Figure 6) and the meniscus far from the closed end, the Myshkis analysis predicts $C_\nu \approx 0.9$ for the lowest harmonic vibration and $C_\nu \approx 2.2$ for the next harmonic. The motion of the latter mode is symmetric about the midplane and compares favorably to the shape change seen in Figure 6.

An early study of the free-jet melt-spinning process, a process whose puddle is not constrained by a nozzle ($G \rightarrow \infty$), attributes periodic variations in the ribbon *width* to capillary oscillations of the puddle, invoking the inviscid sphere capillary oscillations as a model.[30] A more recent study of free-jet spinning makes similar observations about ribbon width variations, relating these oscillations to a transition from amorphous to crystalline microstructures.[5] In neither case are cross-stream waves reported. It may be that oscillation of the less constrained free-jet puddle leads to width variations rather than the thickness variations seen in the planar-flow process. In any case, both reports argue the importance of capillary puddle oscillations.

Direct observation of the actual formation mechanism of the craters and troughs of Figure 2 is not possible. Nevertheless, we speculate that deformation due to the oscillation may allow air to be captured at the USM, probably as a thin film that subsequently collapses and leaves the craters seen on the wheel side. The trough on the air side would then arise as a consequence of the reduced heat transfer, which depends on the mode of film collapse, the net effect being slower solidification over the captured insulating air and, hence, thinner ribbon. This mechanism, although not yet experimentally confirmed, is similar to what has been proposed elsewhere.[12,30] Also, in coating flows, air films between a coating liquid and a substrate are known to be unstable and break into irregular sized bubbles,[31] in much the same manner that we envision this perhaps occurring in this casting flow.

The evidence presented in this article links the cross wave to a capillary oscillation of the puddle. As a natural oscillation, it can be said to be the source of the product defect. The energy for the oscillation can come from any disturbances in the system, but the most likely origin is the moving substrate. The puddle filters input frequencies and outputs its natural frequency. Natural oscillations of the puddle cause the cross wave.

VIII. CONCLUSIONS

Thickness variations on three disparate length scales, observed in aluminum-alloy ribbon solidified by the PFMS process, are related to three different sources of time dependence. The slowest time variation is a gradual change that occurs over the duration of the cast (3 seconds), while the other two time variations are time periodic (10 and 1000 Hz). Length scales naturally correspond to these time scales through the wheel-speed U. The two slowest thickness

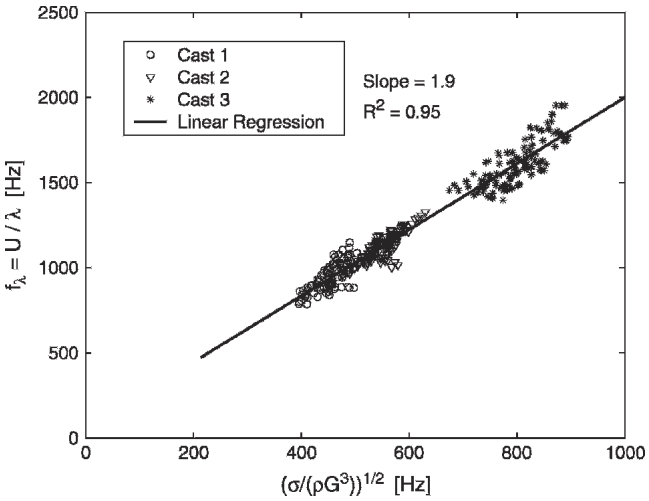

Fig. 8—Pointwise data. Progression with time is from left to right within each of the three data sets.

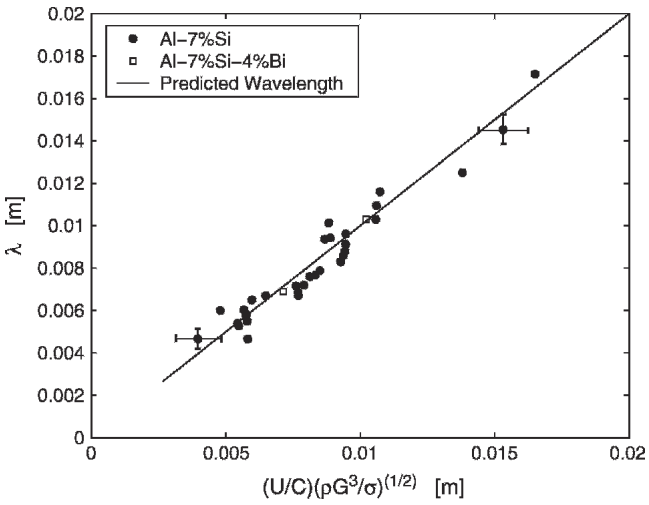

Fig. 9—Predicted wavelength compared with experimental values. All data fall within the 10 pct error bars for cast-averaged *G*.

variations relate to details particular to our casting machine (wheel shape and heatup), while the third is largely apparatus independent (capillary/inertial vibration). This apparatus independence justifies our emphasis on the cross wave.

The key difference between the spatially periodic variations is the dependence of wavelength on wheel speed. Two classes of transfer mechanism, template transfer and pulse transfer, are introduced to distinguish features whose wavelengths are independent of speed (template transfer) and those whose wavelengths are proportional to speed (pulse transfer).

On the longest length scale, on the order 30 m, the gradual thinning of ribbon from beginning to end is caused by the gradual shrinking of the gap (on average), which offers increased hydrodynamic resistance to the flow and, hence, results in lower flow rates. This effect is fully understood and can be compensated for by a preprogrammed increasing head of pressure.

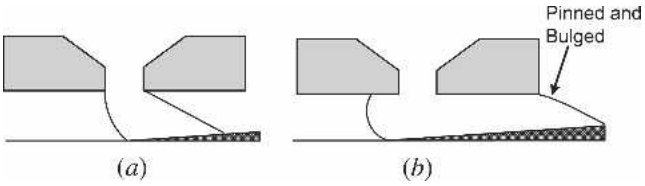

Fig. 10—(*a*) Puddle position during low overpressure casts. (*b*) Puddle positions during nominally pure A1 casts.

On the middle length scale, the circumference of the substrate wheel (about 3 m), the spatially periodic thinning and thickening of the ribbon is caused by the hills and valleys of the wheel as they pass underneath the nozzle. The puddle moves with a time-periodic component corresponding precisely to the spatial wavelength of these spatial variations. This feature is thus well understood as the forcing of the gap $G(t)$ at a frequency of about 10 Hz. The wavelength of this feature is independent of the wheel speed and, hence, represents a template-transfer mechanism.

On the smallest scale of interest in this article, one observes dramatic thickness variations with wavelengths on the order of 1 cm. These cross waves are often viewed as defects. This local thinning shows up as a line of craters on the wheel side with a corresponding trough on the air side. The wavelength is found to depend linearly on speed and, hence, corresponds to a pulse-transfer mechanism. Furthermore, the wavelengths are identified with a spectral peak in puddle vibrations on the order of 1000 Hz. A correlation of the feature with the inviscid capillary oscillations of the puddle demonstrates that it is a natural frequency of the puddle, akin to the oscillations of an inviscid sphere or the vibrations of a meniscus in a slot.

The cross-wave defect is not observed under all conditions. Casting at low *G* or low *U* and, in Al-Si casts, at low Si content suppresses the cross wave. With the exception of the effect of *U*, common among these influences is the degree to which the puddle is constrained. A sufficiently constrained puddle will not oscillate. On the other hand, the influence of *U* may have more to do with the excitation of the puddle. Sufficient excitation is needed for oscillations.

ACKNOWLEDGMENTS

Experiments were supported by NSF Grant Nos. DMI-0124730 and DMI-0423791. The authors thank Dr. M. Vogel for help with the image analysis and P. Wiechecki for help with the experiments. Also, we thank Dr. Steve Weinstein (Eastman Kodak) for many useful discussions. We thank ALCOA and KBAlloys Inc. for supplying materials for these experiments.

APPENDIX

Time-dependent behavior of gap height

Because of the large radius of our substrate ($R_W = 0.45$ m), the thermal expansion of the wheel for even a modest temperature increase ($\Delta T_W > 50$ °C for 1 kg of aluminum) is

Table V. Cast-Averaged Data and Control Parameters for Data Appearing in the Article: Casts (1) through (3) Correspond to Figure 8; Casts TBFA 03-01 through TBSP05-23 Appear in Figure 9; and the Final Ten Casts Appear in Figure 11

Cast ID	T (mm)	U (m s^{-1})	ΔP (Pa)	G (mm)	λ (mm)
TBSU02_21*	0.13	10.5	2900	0.93	7.2
TBFA03_1	0.138	8.83	2497	1.34	11.6
TBFA03_2	0.15	8.77	2791	1.34	11
TBFA03_4	0.133	8.86	2587	1.33	10.3
TBSP03_2	0.112	8.66	3922	0.85	5.3
TBSP03_4	0.122	8.92	3888	0.86	6
TBSP03_5	0.131	8.9	4097	0.87	5.7
TBSP03_8	0.123	8.87	4182	0.85	5.3
TBSP03_26	0.173	8.81	3810	1.16	10.1
TBSU02_10	0.142	10.68	4375	1.04	8.8
TBSU03_10	0.14	8.8	4300	0.89	4.6
TBSU03_16	0.156	8.77	3455	1.1	7.6
TBSU03_23	0.195	8.81	3579	1.16	9.4
TBSU03_25(1)	0.161	8.74	3290	1.16	9.4
TBSU03_28(2)	0.179	8.73	3689	1.15	7.9
TBSU04_11	0.116	11.93	4044	0.86	7.2
TBSU04_14	0.243	5.94	4479	0.88	4.7
TBSU04_16	0.093	13.96	4763	0.77	7.7
TBSU04_24	0.131	11.87	4867	0.87	6.9
TBSU04_25	0.159	8.8	4437	0.88	5.5
TBSU04_26	0.211	7.09	3977	0.89	6
TBSU04_28	0.066	11.94	2157	0.73	6.7
TBSU04_31	0.126	11.9	4348	0.87	6.7
TBFA02_3	0.131	9.46	4278	0.82	5.9
TBFA02_6	0.15	9.51	4100	1.17	9.6
TBFA04_13	0.185	7.1	2869	1.41	8.6
TBFA04_14	0.171	7.01	2723	1.41	8.3
TBFA04_15	0.18	7.2	3013	1.4	9.1
TBSP05_5	0.121	11.92	3114	1.37	14.5
TBSP05_10**	0.119	8.59	1639	0.75	6.8
TBSP05_11**	0.109	8.37	1756	1.1	10.3
TBSP05_12	0.119	8.59	1639	0.75	6.8
TBSP05_13(3)	0.16	8.5	3500	0.88	6.5
TBSP05_23†	0.17	11.9	2300	1.38	1.7
MKSP00_23	0.219	7.55	4072	1.22	7.2
MKSP00_25	0.197	7.12	4078	0.96	5.2
MKSU00_8	0.222	8.76	3606	1.13	7.2
BRFA99_18	0.136	8.4	2754	0.7	3.9
BRSU99_16	0.16	6.68	3800	1.1	6.2
BRSU99_22	0.16	7.8	4100	0.86	4.7
BRSU99_8	0.11	9.4	4100	1.02	5.7
MKSP00_10	0.16	8.8	3700	1.3	7.5
MKSP00_12	0.25	8.3	7500	1.2	7.2
MKSP00_21	0.2	7.8	4000	1.3	8

*B = 3 mm.
**Al-7 pct, Si-4 pct Bi.
†W = 25 mm.

quite significant (of the order of 0.3 G) when compared to our small gap sizes ($G \approx 1$ mm).

The most accurate measurement of this shrinking gap uses real-time measurements *via* high-speed photography of a run-out meter (pointwise data). Such measurement is time-consuming and not practical for every cast. Therefore, an approximate method that accounts for gap shrinkage (wheel expansion) has been developed and validated against the direct measurements, as described subsequently.

A set of experiments was performed where an average rate of substrate expansion is measured under different casting conditions. This rate of gap shrinkage $\left(\frac{dG}{dt}\right)_{avg}$ is then applied to each cast in order to get $G(t)$, given as

$$G(t) = G(0) - \left(\frac{dG}{dt}\right)_{avg} t \qquad [6]$$

where $G(0)$ is the initial gap setting. This method neglects the out of roundness of the substrate, but still gives a good estimate of the gap shrinkage with time. The calculated values of $G(t)$ are then used to scale the pointwise data.

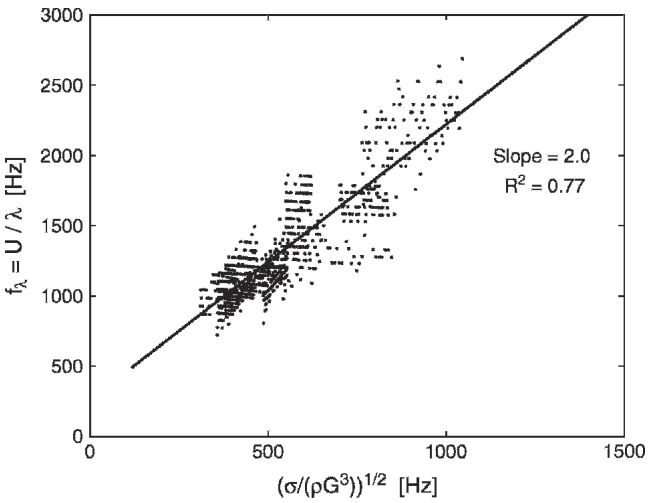

Fig. 11—Cross-stream defect frequency plotted against capillary frequency, without accounting for substrate out of roundness, resulting in large scatter in experimental data.

Using pointwise data (Figure 8) shows the best correlation of the experimental data. These experimental conditions vary to a limited extent only throughout a particular cast, however. In contrast, in Figure 9, σ, U, G, and λ all vary in the raw data that correlates. Figure 9, however, uses Eq. [6] to calculate a cast-averaged value of G. The greater uncertainty due to the approximation seems to be compensated for by averaging over a large number of data (*e.g.,* 200 points for a 30-m ribbon) with the end result that Figures 8 and 9 present correlations of similar quality (R^2 factor).

On the other hand, the data that comprise Figures 8 and 9 all come from the same laboratory, the same apparatus, and, indeed, all were taken by the same team of investigators. Other data taken on a different casting apparatus, with different human operators and using a different technique to set and measure the hot gap at the start of a cast, are available in our archives. We present these data here (1) to convey a sense of how prevalent cross waves are and how they correlate to the capillary oscillations under quite diverse conditions and (2) to illustrate how using Eq. [6] to scale pointwise data leads to large scatter in the data.

Figure 11 shows the results for approximately ten casts from our archives. Notice that the scatter in the data increases as G becomes smaller (moving to the right on the x-axis). This trend is expected since the wheel out of roundness is a more significant variation in G at lower gap heights. The experimental constant ($C \approx 2$) based on the slope of the data presented here using the calculated $G(t)$ are in reasonable agreement with Figure 8, where $G(t)$ was measured from the run-out meter. As expected, however, the correlation in Figure 11 is not as good (R^2 of 0.77 *vs* 0.95).

REFERENCES

1. Nucor Steel's twin-roll steel casting process Castrip: www.castrip.com, 2002.
2. T. Praisner, J.-J. Chen, and A.A. Tseng: *Metall. Mater. Trans. B*, 1995, vol. 26B, pp. 1199-208.
3. T. Haga and S. Suzuki: *J. Mater. Processing Technol.*, 2003, vol. 137, pp. 86-91.
4. P. Wilde and E. Matthys: *Mater. Sci. Eng.*, 1992, vol. 150A, pp. 237-47.
5. R.E. Napolitano and H. Meco: *Metall. Mater. Trans. A*, 2004, vol. 35A, pp. 1539-53.
6. S. Kavesh: in *Metallic Glasses*, J.H. Gilman and H.J. Leamy, eds., ASM, Metals Park, OH, 1978, pp. 36-73.
7. H. Jones: in *Metallic Glasses*, J.H. Gilman and H.J. Leamy, eds., Institution of Metallurgists, London, 1982, pp. 1-83.
8. S. Huang: *Proc. 4th Int. Conf. on Rapidly Quenched Metals*, Sendai, Japan, The Japan Institute of Metals, Sendai, Japan, 1981, pp. 65-68.
9. P.H. Steen and C. Karcher: *Ann. Rev. Fluid Mech.*, 1997, vol. 29, pp. 373-97.
10. J.-J. Chen and A.A. Tseng: *MED Manufacturing Science and Engineering*, ASME, 1999, vol. 10, pp. 79-85.
11. M. Bussmann, J. Mostaghami, D. Kirk, and J. Graydon: *Int. J. Heat Mass Transfer*, 2002, vol. 45, pp. 3997-4010.
12. S.C. Huang and H.C. Fiedler: *Metall. Trans. A*, 1981, vol. 12A, pp. 1107-12.
13. J.K. Carpenter and P.H. Steen: *J. Mater. Sci.*, 1992, vol. 27, pp. 215-25.
14. J. Legresy, Y. Brechet, and P. Menet: *Scripta Mater.*, 1997, vol. 36 (12), pp. 1437-42.
15. T. Haga and S. Suzuki: *J. Mater. Proc. Technol.*, 2003, vol. 137, pp. 92-95.
16. B. Thomas, D. Lui, and B. Ho: in *Sensors and Modeling in Materials Processing: Techniques and Applications*, S. Viswanathan, R. Reddy, and J. Malas eds., TMS, Warrendale, PA, 1997, pp. 117-42.
17. A. Badri, T. Natarajan, C. Snyder, K. Powers, F. Mannion, M. Byrne, and A. Cramb: *Metall. Mater. Trans. B*, 2005, vol. 36B, pp. 373-83.
18. S. Weinstein and R. Ruschak: *Ann. Rev. Fluid Mech.*, 2004, vol. 36, pp. 29-53.
19. F. Durst and H.G. Wagner: in *Liquid Film Coating*, S.F. Kistler and P.M. Schweizer, eds. Chapman and Hall, London, 1997, pp. 401-26.
20. J.K. Carpenter and P.H. Steen: *Int. J. Heat Mass Transfer*, 1997, vol. 40 (9), pp. 1993-2007.
21. M.B. Kahn: Master's Thesis, Cornell University, Ithaca, NY, 2000.
22. B.L. Reed: Ph.D. Thesis, Cornell University, Ithaca, NY, 2001.
23. J. Kukura, K. Ford, A. Singh, P.H. Steen, and T. Ibaraki: in *Simulations of Materials Processing: Theory, Methods, and Applications*, S.F. Shen and P. Dawson, eds., Balkema, Rotterdam, 1995, pp. 1153-57.
24. T. Ibaraki: Master's Thesis, Cornell University, Ithaca, NY, 1996.
25. B.J. Lowry: *J. Coll. Int. Sci.*, 1996, vol. 176, pp. 284-97.
26. A.M. Korol'kov: *Casting Properties of Metals and Alloys*, Consultants Bureau, New York, NY, 1963.
27. L. Goumiri, J.C. Joud, P. Desre, and J.M. Hicter: *Surf. Sci.*, 1979, vol. 83 (2), pp. 471-86.
28. H. Lamb: *Hydrodynamics,* 6th ed., Cambridge University Press, Cambridge, United Kingdom, 1932.
29. A. Myshkis, V. Babskii, N. Kopachevskii, L. Slobozhanin, and A. Tyuptsov: *Low-Gravity Fluid Mechanics*, Springer-Verlag, Berlin, 1987, pp. 349-55.
30. T.R. Anthony and H.E. Cline: *J. Appl. Phys.*, 1979, vol. 50 (1), pp. 245-54.
31. S. Kistler: in *Wettability*, J. Berg, ed., M. Dekker, New York, NY, 1993, pp. 311-429.